


 Cite this: *RSC Adv.*, 2020, **10**, 4211

## Synthesis and model simulation of the hexagonal to circular transition of perovskite cesium lead halide nanosheets by rapidly changing the temperature†

 Zhong-Hai Lin, <sup>a</sup> Fei Gao,<sup>a</sup> Hong Chen,<sup>a</sup> Jia-Yi Lei,<sup>a</sup> Zhi Yang, <sup>b</sup> Jun-Wei Cai,<sup>a</sup> Ping-Jian Wang<sup>a</sup> and Ming-Qiang Wang<sup>b</sup>

Lead halide perovskites have emerged as promising optoelectronic materials due to their excellent efficiencies in photovoltaic and light-emitting applications.  $\text{CsPbBr}_3$  is a kind of all-inorganic perovskite that exhibits higher stability. Here, we report the synthesis of hexagonal and circular all-inorganic  $\text{CsPbBr}_3$  perovskite nanoplates by changing the reaction temperature. As time goes on, the different reaction temperatures play an important role in determining the shape and size. We use first-principles to explicate the formation of hexagonal nanoplates. Meanwhile, a model is built and the calculation of the properties is conducted. In brief, a method to directly and conveniently synthesize all-inorganic  $\text{CsPbBr}_3$  is proposed.

 Received 9th December 2019  
 Accepted 12th January 2020

DOI: 10.1039/c9ra10312k

[rsc.li/rsc-advances](http://rsc.li/rsc-advances)

### 1 Introduction

The past few years have witnessed important progress demonstrating the outstanding optoelectronic characteristics of halide perovskite materials, which are emerging as one of the most promising materials for photovoltaic devices,<sup>1–4</sup> LEDs,<sup>5,6</sup> photodetectors<sup>7–9</sup> and lasers.<sup>10,11</sup> Halide perovskite materials exhibit an  $\text{ABX}_3$  crystal structure, and include hybrid organic–inorganic and all-inorganic perovskite materials. The hybrid organic–inorganic lead halide perovskite materials such as  $\text{CH}_3\text{NH}_3\text{PbX}_3$  ( $\text{X} = \text{Cl}, \text{Br}, \text{I}$ ) have made rapid progress and have attracted intense attention from the research community due to their power conversion efficiency.<sup>12–14</sup> However, the stability issue of hybrid organic–inorganic halide perovskite materials has become a crucial problem. Compared to hybrid organic–inorganic halide perovskites, all-inorganic perovskites exhibit higher stability and present huge potential in various optoelectronic applications.

With similarly high optoelectronic quality, such as small exciton binding energy, high thermal stability, and balanced electron and hole mobility lifetime, all-inorganic perovskites like  $\text{CsPbX}_3$  present a high quantum yield, narrow emission bandwidths, tunable photoluminescence (PL) emission spectra,

and higher stability compared with  $\text{CH}_3\text{NH}_3\text{PbX}_3$ , which makes them promising for optoelectronic applications.<sup>15–17</sup> Recently, high-quality  $\text{CsPbX}_3$  nanocrystals with a cubic shape were successfully synthesized, and demonstrated superior optoelectronic properties over the traditional metal–chalcogenide quantum dots (QDs).<sup>18–20</sup> Besides, other forms of  $\text{CsPbX}_3$  nanostructures like 1D nanowires and 2D nanoplates have attracted enormous attention because of their respective physical features.<sup>21,22</sup> Quasi-two-dimensional (2D) nanoplates are attractive mainly due to their exceptional photophysical properties, such as increased exciton binding energy, enhanced absorption cross sections with respect to the bulk, low threshold stimulated emission, and notable optical nonlinearities.<sup>23,24</sup> The preparation and characterization of 2D nanoplates has invited more detailed studies toward better synthetic control and full understanding of their excellent optoelectronic characteristics. In this perspective, we aim to provoke new breakthroughs in the preparation and characterization of 2D nanoplates.

This paper reports the colloidal synthesis of two-dimensional all-inorganic cesium lead bromine ( $\text{CsPbBr}_3$ ) perovskite nanoplates with lateral sizes up to a few hundred nanometers. The morphology changes from hexagons to circles. The PL color also changes from blue to green.

### 2 Experimental

#### 2.1 Synthesis of $\text{CsPbBr}_3$ hexagonal-circular nanoplates

In this paper, the synthesis of hexagonal and circular  $\text{CsPbBr}_3$  nanosheets by varying the reaction temperature to room temperature was put forward. The different reactant temperature is critical in the reactant formation process because this

<sup>a</sup>Key Laboratory of Intelligent Information Processing in Universities of Shandong, Shandong Technology and Business University, Yantai, 264005, China. E-mail: zhlin@sdtbu.edu.cn

<sup>b</sup>Electronic Materials Research Laboratory (EMRL), Key Laboratory of Education Ministry, International Center for Dielectric Research (ICDR), Xi'an Jiaotong University, Xi'an, 710049, China

† Electronic supplementary information (ESI) available. See DOI: 10.1039/c9ra10312k



affects their shapes. Furthermore, the sudden cooling process is crucial to nucleation and growth.<sup>25</sup> Therefore, we reduced the reactant temperature abruptly after mixing the prepared precursor well. This unique process of temperature adjustment could ensure the different shapes of the nanosheets. During the synthesis process, we firstly synthesized the Br precursor by mixing TBABr, OA, OAm and ODE at a temperature of 120 °C and protected the mixed precursor under Ar airflow. In a typical synthesis of  $\text{CsPbBr}_3$  hexagonal nanoplates, the mixed precursor (Cs-OA, Pb-OA) was put under Ar airflow at 100 °C. Then, the Br precursor was injected rapidly and the temperature was swiftly changed to room temperature. The approach of synthesizing  $\text{CsPbBr}_3$  circular nanoplates was similar to the synthesis of  $\text{CsPbBr}_3$  hexagonal nanoplates except for the reaction condition (temperature, time *etc.*).

The specific experimental method is as follows. In a typical synthesis of the Br precursor, 96 mg of TBABr (0.03 mmol), 0.5 mL of OA, 0.5 mL of OAm, and 5 mL of ODE were loaded into a three-neck flask and dried under Ar airflow at 120 °C for 20 min. The mixed precursor was under Ar-protection immediately.

In a typical synthesis of  $\text{CsPbBr}_3$  hexagonal nanoplates, 8.1 mg of  $\text{Cs}_2\text{CO}_3$  (0.025 mmol), 11.5 mg of PbO (0.05 mmol), 0.5 mL of OA, and 10 mL of ODE were loaded into a three-neck flask under Ar airflow at 100 °C for 20 min. After the reaction and drying, the temperature was adjusted to 90 °C, at which point 3 mL of the Br precursor was swiftly injected into the flask by using a syringe. The reaction was maintained for several seconds and then promptly cooled to room temperature using a water bath.

In a typical synthesis of  $\text{CsPbBr}_3$  circular nanoplates, the processing of the Cs-OA and Pb-OA mixed precursors was similar to the synthesis of  $\text{CsPbBr}_3$  hexagonal nanoplates. After the reaction and drying of the Cs-OA and Pb-OA mixed precursors, the temperature was adjusted to 120 °C and 3 mL of the Br precursor was swiftly injected into the flask by using a syringe for several seconds. The reaction mixture was subsequently maintained at 100 °C for several minutes and then promptly cooled to room temperature using a water bath.

## 2.2 Characterization

The crystal phase of the samples was identified by a Rigaku D/max-2400 X-ray diffractometer (XRD) using  $\text{CuK}\alpha$  radiation. Transmission electron microscope (TEM) images, and high-resolution TEM (HRTEM) images were obtained on a JEOL 2100. The optical absorptance spectra were measured by a Jasco-V570 UV-vis-NIR spectrophotometer. Fluorescence experiments were performed with a fluoroSENS 9000 system and WITec Alpha300 R laser-scanning confocal microscope. All measurements were conducted in air. In addition, we used Materials Studio to simulate the model and calculate the surface energy in order to better analyze the results.

## 3 Results and discussion

XRD was used to determine the crystallographic nature of the  $\text{CsPbBr}_3$  perovskite nanoplates. Fig. 1(a) shows the XRD pattern

of the  $\text{CsPbBr}_3$  perovskite nanoplates, where the peaks ( $2\theta = 21.4$  and 30.7) correspond to diffraction from the (110) and (200) facets. The XRD data confirm the formation of  $\text{CsPbBr}_3$  perovskite nanoplates, which is in good agreement with JCPDF#18-0364. Fig. 1(b) shows the HRTEM image, which indicates the existence of a single crystalline structure. The *d*-spacing value of 0.59 nm is consistent with the value for the (200) facet of bulk perovskite  $\text{CsPbBr}_3$ . Fig. 1(c) shows the (100) facet of the  $\text{CsPbBr}_3$  atomic structure. The distance between adjacent Cs atoms should be 0.59 nm, which is in agreement with the calculated lattice constants.<sup>26</sup>

The ionic nature of the metathesis reaction dictates the rapid nucleation and growth kinetics of the resulting nanocrystals.<sup>23</sup> We observed that the nanoplates had different shapes and sizes under different reaction temperatures as time went by. The reaction conducted at 90 °C and with rapid cooling produced mostly hexagonal  $\text{CsPbBr}_3$  perovskite nanoplates (Fig. 2(a)). The reaction conducted at higher temperature and for a longer time presented mostly circular  $\text{CsPbBr}_3$  perovskite nanoplates (Fig. 2(c)). An appropriate increase in temperature is of benefit to nanoplates growth. The ligands absorbed on the edge of the hexagonal nanoplates became unstable when increasing the reaction temperature. In addition, J. J. Urban *et al.*<sup>27</sup> and J. E. Murphy *et al.*<sup>28</sup> have found that the reactant temperature and stable ligands are crucial because they influence the reactivity of the nanoplates. Therefore, the hexagonal nanoplates became circular under higher temperature over time and they became more stable. Moreover, excessive temperature and lower temperature are not conducive to shape formation (Fig. S1 and S2†). The average lateral size of the nanoplates increased from 160 to 200 nm with the morphological change (Fig. 2(b) and (d)). The circular nanoplates also exhibited a quite broad lateral size distribution.

According to the research of J. Shamsi *et al.*,<sup>29</sup> the use of short ligands enables the synthesis of nanoplates with large lateral dimensions, in which the vertical dimension is always in the strong quantum confinement regime. In our synthesis process, the ligands and the changing temperature may be the reason for the formation of hexagonal  $\text{CsPbBr}_3$  perovskite nanoplates. If

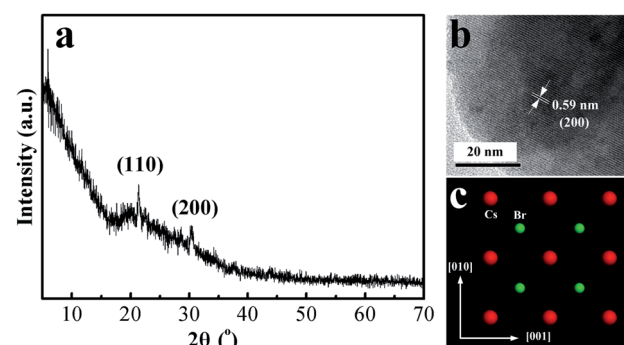


Fig. 1 (a) X-ray diffraction (XRD) pattern of the  $\text{CsPbBr}_3$  perovskite nanoplates. (b) High-resolution transmission electron microscope (HRTEM) image of a single  $\text{CsPbBr}_3$  perovskite nanoplate. (c) Schematic of the (100) facet of the  $\text{CsPbBr}_3$  atomic structure.



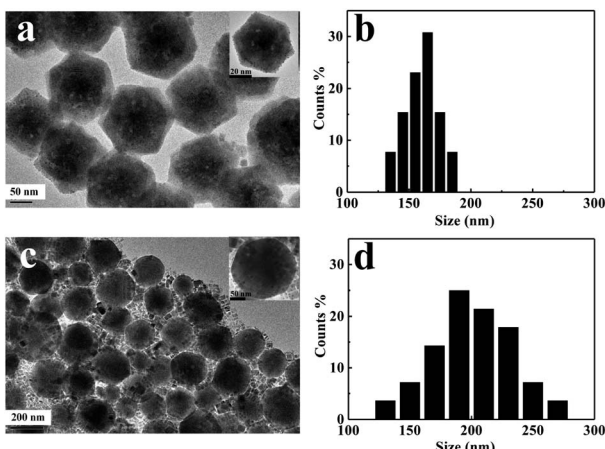


Fig. 2 TEM images and lateral size distribution of the hexagonal (a and b) and circular (c and d)  $\text{CsPbBr}_3$  perovskite nanoplates.

conducted at higher temperature and for a longer time, a  $\text{CsPbBr}_3$  morphology change (hexagon to circle) would be observed because of the solubility equilibrium principle and Ostwald ripening.<sup>30</sup>

Surface energy is an important parameter to characterize the surface properties of materials. It is widely used in the study of surface adsorption, chemical reactions, and strength and fracture of materials. From the perspective of atomic bonding, the surface of the crystal has a strong tendency to interact with atoms or molecules in the environment due to the existence of unsaturated bonds, and electron exchange to saturate the bond.<sup>31</sup> Materials Studio uses an effective and widely used method in material simulation to create a modelling environment that integrates quantum mechanics, molecular mechanics, mesoscopic models, and analytical tools. It is easy to establish and process graphical models for organic and inorganic crystals, polymers, amorphous materials, surfaces and layered structures. Therefore, the simulation of the Materials Studio model and the calculation of surface energy can explain the promoting effect of the ligands on the transverse growth of the (100) plane to some extent.

First of all, we used the calculation GGA-PBE, which is more accurate, to optimize the  $\text{CsPbBr}_3$  crystal cell with a lattice constant of 5.84 Å.<sup>32</sup> In order to improve the computational efficiency, the pseudopotential ultrasound was selected. In this experiment, we selected the cutoff energies of 170 eV, 220 eV, 260 eV and 290 eV, and then optimized the convergence. The  $k$ -point setting varies according to the set quality. According to the quality of optimization, the convergence tolerance will change. Taking the ultra-fine optimized quality with a cut-off of 290 eV as an example, the energy of each atom corresponding to it does not change more than  $5 \times 10^{-6}$  eV, and the residual force per atom is not higher than 0.01 eV Å<sup>-1</sup>. The maximum pressure and maximum displacement are not more than 0.02 GPa and 0.0005 Å, respectively. The remaining optimization parameters can be rectified according to requirements.

Table 1 shows the crystal parameters after calculation under several optimized parameters. Through several experiments, it

was found that the lattice parameters are mostly stable at about 5.93 Å when the cut-off energy is above 260 eV. After optimization, the lattice constant of the unit cell became 5.93 Å. The optimized unit cell was close to the size of the nanocrystalline cell, and it had good maneuverability. Then, the optimized unit cell (100) plane, (011) plane, and (200) plane should be cut. In order to meet the requirement of no external interaction between the two atoms, a certain thickness of vacuum layer should be added.<sup>33</sup> For convenience, the thickness of the vacuum layer was 20 Å.

H. X. Xiao *et al.*<sup>33</sup> proposed a relatively simple scheme for calculating surface energy. According to Gibbs surface thermodynamics, the total energy  $U_{\text{total}}$  of the surface of a plane system satisfies eqn (1):

$$U_{\text{total}} = U + U^\alpha \quad (1)$$

where  $U$  and  $U^\alpha$  represent the energy without surface influence and the energy of the surface, respectively. If the former two are known, the surface energy  $U^\alpha$  can be obtained, and then the surface energy  $\alpha$  of the solid material can be obtained by dividing by the surface area.

According to this scheme,  $U_1$  is the total energy of a slice with thickness  $A$  after iteration, and  $U_2$  is the total energy of a slice with thickness  $2A$ , as shown in Fig. 3(a), which can be used to obtain the surface energy per unit area after subtraction.

$$E_{\text{sl}} = -\frac{U_2 - 2U_1}{2S} \quad (2)$$

In eqn (2),  $S$  represents the area of the tangent plane, and  $U_1$  and  $U_2$  are the total energy of a single layer thick slice and a double layer thick slice, respectively.

The surface energy of the multilayer thickness can be expressed as eqn (3):

$$E_s = -\frac{U_s - NU_1}{2(N-1)S} \quad (3)$$

where  $U_s$  calculates the total energy of the thickness and  $N$  represents a multiple of the difference between the thicknesses of the first two.

Table 2 shows the calculated surface energy of each crystal plane. In crystallography, the growth of crystals always follows a rule that the crystal face that has larger surface energy always grows faster and gradually disappears, and the final crystal is composed of a low surface energy crystal face with a slow growth rate.<sup>34</sup> From Table 2, we obtain that  $|E_{(200)}| > |E_{(011)}| > |E_{(100)}|$ .

Table 1 Crystal parameters and energy levels under different optimized settings

Optimized quality/cutting energy (eV)	Crystal parameter (Å)	Energy (eV)
Coarse/170	6.056	-3313.016
Medium/220	5.969	-3312.974
Fine/260	5.926	-3312.905
Ultra-fine/290	5.927	-3312.911



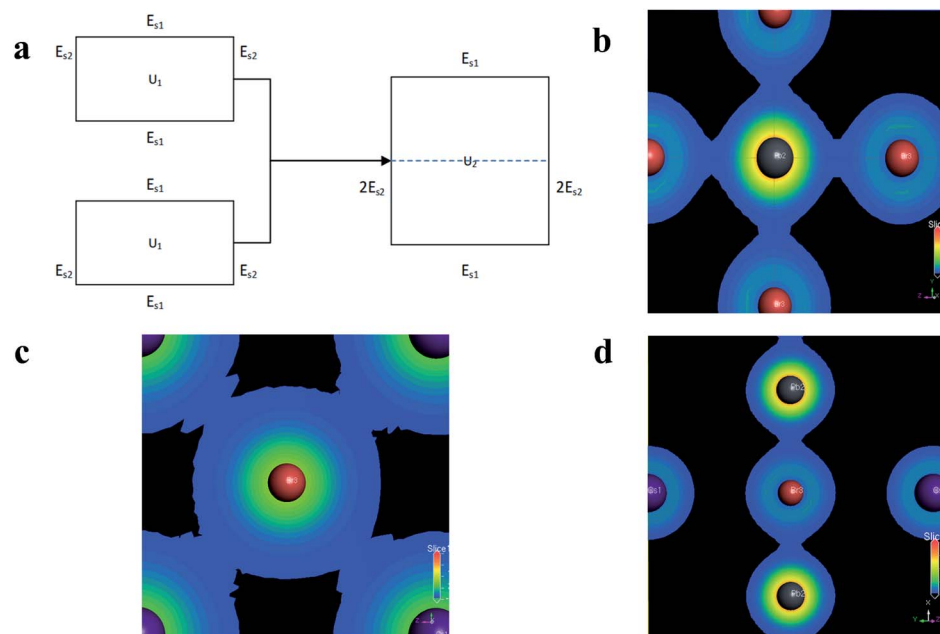


Fig. 3 (a) Schematic diagram of the surface energy calculation. (b) The (200) surface charge density distribution. (c) The (100) surface charge density distribution. (d) The (011) surface charge density distribution.

Therefore, the growth rates of the (200) plane and (011) plane are faster.

In order to better understand this result, from the thermodynamic and chemical point of view, TBA has four butyl groups, so it can't form a strong ionic hydrogen bond. Since the (100) plane has less energy, it will tend to combine with stable TBA. Q. A. Akkerman *et al.*<sup>35</sup> found that TBA-X is unable to form hydrogen bonds and has weak ionic properties, so it has obvious unidirectional substitution characteristics in anion exchange of perovskites. On the contrary, the surfaces of OA-Pb and OA-Cs have strong Coulomb forces, which makes the perovskite grow on the (200) plane and (011) plane along the direction of the  $\langle 100 \rangle$  crystal.

In addition, because the surface energy of the (011) plane is smaller than that of the (200) plane, its growth rate is slower. As the adsorption growth proceeds, the (200) plane area will become smaller and smaller, so the final nanoplates will be exposed mainly as the (100) plane. Combined with Fig. 1(a) and (b), the peak value of the (110) plane is large because preferential growth can occur on the surface of the perovskite. In thermodynamics, the thermodynamic equilibrium of the crystal follows the Wulff-construction rule; that is, the sum of the

surface energy of each crystal surface is the minimum. Therefore, the free growing crystal surface in the solution environment is generally caused by the exposure of the crystal with low surface energy in the low miller index surface.<sup>36</sup> It can be seen from Fig. 1(c) that preferentially grown  $\text{CsPbBr}_3$  nanoplates are cubic, so we calculated the surface energies of the (100) plane and (110) plane with low index single crystal surfaces using Materials Studio. Table 3 shows the calculated surface energy of each crystal plane, where the energy of the (100) plane of  $\text{CsBr}$  is  $203.875 \text{ mJ m}^{-2}$ , and the energy of the (100) plane of  $\text{PbBr}_2$  is  $254.427 \text{ mJ m}^{-2}$ . Either way, the surface energy obtained by cutting can satisfy  $|E_{(110)}| > |E_{(100)}|$ . Since the surface energy of the (110) plane is larger than that of the (100) plane, the (110) plane grows faster, the exposed surface is smaller, and the (100) plane grows more easily because of the smaller surface energy. This is probably because of the restriction of tetrabutylammonium, oleic acid and oleyl amine on the (100) plane and (110) plane in the experiment, meaning that the  $\text{CsPbBr}_3$  nanosheets displayed under TEM are mainly composed of 6  $\{100\}$  exposed crystals. The 6  $\{100\}$  and 12  $\{110\}$  exposed crystal faces are formed, so the  $\text{CsPbBr}_3$  nanosheet becomes a hexagonal shape that is truncated along the  $\{110\}$  edge. Ostwald ripening occurs,

Table 2 Surface energy of  $\text{CsPbBr}_3$  crystal faces

	Single layer (eV)	Two layers (eV)	Superficial area ( $\text{\AA}^2$ )	Energy (eV $\text{\AA}^{-2}$ )
(200)	-5706.083	-9018.873	35.110	-34.083
(100)	-4231.014	-7543.790	35.110	-13.077
(011)	-9200.088	-15 825.039	49.653	-25.931



Table 3 Cleavage energy, relaxation energy and surface energy under different cut surfaces ( $\text{mJ m}^{-2}$ )

(110) plane				(100) plane		
Energy	PbBr	Cs	Br (type A)	Br (type B)	CsBr	PbBr <sub>2</sub>
$E_s^{(\text{unrel})}$	482.743	482.743	389.551	574.318	257.266	257.266
$E_{\text{rel}}$	-43.478	-180.883	-41.508	-235.810	-53.391	-2.839
$E_{\text{surface}}$	439.265	301.860	348.043	338.508	203.875	254.427

and the particle radius of the  $\text{CsPbBr}_3$  solute in the solution gradually increases during growth.<sup>37</sup> The results of the above corollary are consistent with the smaller peaks of the (200) plane in Fig. 1(a). Y. Zhao *et al.*<sup>38</sup> also found a similar phenomenon. Adding  $\text{MgCl}_2$  to the solution of  $\text{MAPbI}_2\text{Br}$  precursor changed the morphology of the  $\text{MAPbI}_2\text{Br}$  crystals and flaky crystals appeared. The charge density calculated by the first-principles method can be used to describe the bonding properties of the solid.<sup>39</sup> The surface charge densities of the (200) plane, the (100) plane, and the (011) plane are shown in Fig. 3(b)–(d). The surface density of the (011) plane is smaller from Fig. 3. The surface energy of the crystals is also related to the arrangement of surface atoms, and a denser atomic surface has a smaller surface energy.<sup>40</sup> According to this rule, the surface atoms of the (011) plane have an unsaturated valence bond in the outward direction. In contrast, the (100) plane has a smaller surface energy. This proves that the surface energy of the (011) surface is larger and the surface energy of the (100) surface is smaller, resulting in geometric growth of the perovskite. Similarly, the (200) plane is much larger because there is a strong covalent bond perpendicular to the (020) plane.<sup>31</sup>

Reaction under different conditions resulted in a blue-shift of the  $\text{CsPbBr}_3$  perovskite nanoplate absorption (Fig. 4(a)). These absorption peaks are directly related to the reaction

temperature and time. We observed both nucleation and growth processes in our synthesis. The efficient separation of nucleation and growth is essential in the synthesis.<sup>25</sup> At the nucleation stage of 120 °C, since the size of the particles was small and uniform, the absorption was concentrated as shown in the peak of the first curve (Fig. 4(a)). As the temperature became 100 °C, the nanoplates became hexagonal with the particle radius gradually increasing. This was the growth stage. An absorption peak is not obvious because of Ostwald ripening, as shown in the second and third curves (Fig. 4(a)). Meanwhile, the PL broadens (Fig. 4(b)). We hypothesize that this phenomenon arises from the different thicknesses by an integer number of  $\text{CsPbBr}_3$  perovskite unit cells. Specifically, we measured the peaks at 435 and 468 nm, which may be assigned to a thickness of 2 and 3  $\text{CsPbBr}_3$  perovskite unit cells. The successful growth of  $\text{CsPbBr}_3$  perovskite nanoplates from hexagons to circles allows us to continuously tune the band gaps. The three components in Fig. 4(c) correspond to the three curves of Fig. 4(a), respectively. A color change was observed from blue to green when excited by an ultraviolet LED (Fig. 4(c)). A laser-scanning confocal microscope was used to obtain the room-temperature PL images ( $\lambda = 365 \text{ nm}$ ). The test pattern in Fig. 4(b) is consistent with the above test results.

## 4 Conclusions

In summary, we have developed an approach to directly synthesize hexagonal and circular all-inorganic  $\text{CsPbBr}_3$  perovskite nanoplates. The  $\text{CsPbBr}_3$  perovskite nanoplates exhibit lateral sizes from 160 to 200 nm with a morphological change (from hexagons to circles) on varying the reaction conditions. The sudden cooling process is crucial to nucleation and growth. The ligands and the changing temperature could be the reason for the formation of hexagonal  $\text{CsPbBr}_3$  perovskite nanoplates. We use first-principles to explicate the formation of hexagonal nanoplates. The large lateral dimensions of the  $\text{CsPbBr}_3$  perovskite nanoplates obtained allow us to identify the crystal phase by means of XRD and HRTEM.  $\text{CsPbBr}_3$  perovskite nanoplates are emerging as one of the most promising materials for photovoltaic devices, LEDs, photodetectors and lasers.

## Funding

The authors gratefully acknowledge financial support from the National Natural Science Foundation of China (NSFC) (616041225, 61403236, 61572296, 61174007, 61472227,

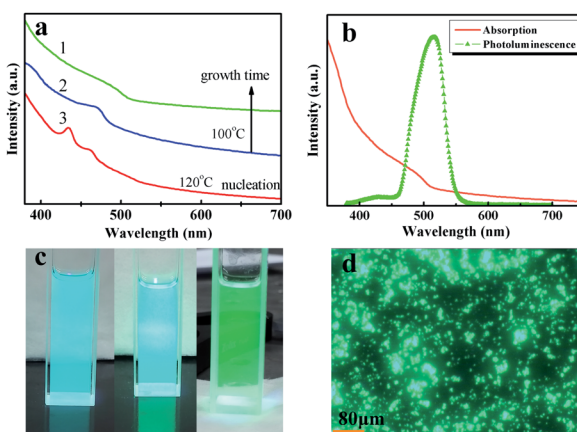


Fig. 4 (a) The optical absorption of  $\text{CsPbBr}_3$  perovskite nanoplates. (b) The optical absorption and PL emission spectra of  $\text{CsPbBr}_3$  perovskite nanoplates. (c) Hexagonal to circular  $\text{CsPbBr}_3$  perovskite nanoplates under excitation using an ultraviolet LED ( $5 \text{ mW cm}^{-2}$ ,  $\lambda = 365 \text{ nm}$ ) at room temperature. (d) The room-temperature PL image of hexagonal  $\text{CsPbBr}_3$  perovskite nanoplates, obtained using a laser-scanning confocal microscope.



61672327, 61804089), the project of Shandong Province Higher Educational and Technology Program (J16LN04), the Yantai key R&D Program (2017ZH064, 2018XSCC033, 2018XSCC034) and the Shandong provincial Science and technology support program of youth innovation team in colleges (2019KJN041).

## Conflicts of interest

There are no conflicts of interest to declare.

## Acknowledgements

The authors would like to thank Zhi Yang from Xi'an Jiaotong University for the great help with the XRD and HRTEM tests.

## References

- 1 J. Xu, O. Voznyy, M. Liu, A. R. Kirmani, G. Walters, R. Munir, M. Abdelsamie, A. H. Proppe, A. Sarkar, M. Y. Wei, B. Sun, M. Liu, O. Ouellette, R. Quintero-Bermudez, J. Li, J. Fan, L. Quan, P. Todorovic, H. Tan, S. Hoogland, S. O. Kelley, M. Stefk, A. Amassian and E. H. Sargent, 2D matrix engineering for homogeneous quantum dot coupling in photovoltaic solids, *Nat. Nanotechnol.*, 2018, **13**, 13455–13457.
- 2 H. Tsai, R. Asadpour and J. C. Blancon, Light-induced lattice expansion leads to high-efficiency perovskite solar cells, *Science*, 2018, **360**, 67–70.
- 3 D. Liu, Z. Hu, W. Hu, P. Wangyang, K. Yu, M. Wen, Z. Zu, J. Liu, M. Wang, W. Chen, M. Zhou, X. Tang and Z. Zang, Two-step method for preparing all-inorganic  $\text{CsPbBr}_3$  perovskite film and its photoelectric detection application, *Mater. Lett.*, 2017, **186**, 243–246.
- 4 N. Ueoka, T. Oku and A. Suzuki, Additive effects of alkali metals on Cu-modified  $\text{CH}_3\text{NH}_3\text{PbI}_3$ -delta Cl delta photovoltaic devices, *RSC Adv.*, 2019, **9**, 24231–24240.
- 5 J. Z. Song, T. Fang, J. H. Li, L. M. Xu, F. J. Zhang, B. N. Han, Q. S. Shan and H. B. Zeng, Organic-Inorganic Hybrid Passivation Enables Perovskite QLEDs with an EQE of 16.48%, *Adv. Mater.*, 2018, **30**, 1805409.
- 6 L. Xu, S. Yuan, H. Zeng and J. Song, A comprehensive review of doping in perovskite nanocrystals/quantum dots: evolution of structure, electronics, optics, and light-emitting diodes, *Mater. Today Nano*, 2019, **6**, 10036.
- 7 Y. Wang, U. Ramesh, C. K. A. Nyamekye, B. J. Ryan, R. D. Nelson, A. M. Alebri, U. H. Hamdeh, A. Hadi, E. A. Smith and M. G. Panthani, Synthesis of germanium nanocrystals from solid-state disproportionation of a chloride-derived germania glass, *Chem. Commun.*, 2019, **55**, 6102–6105.
- 8 M. Kumar, H.-S. Kim, D.-Y. Park, M.-S. Jeong and J. Kim, Wide channel broadband  $\text{CH}_3\text{NH}_3\text{PbI}_3/\text{SnS}$  hybrid photodetector: breaking the limit of bandgap energy operation, *RSC Adv.*, 2019, **8**, 23206–23212.
- 9 C.-C. Wang, S.-H. Yuan, S.-L. Ou, S.-Y. Huang, K.-Y. Lin, Y.-A. Chen, P.-W. Hsiao and D.-S. Wu, Growth and characterization of co-sputtered aluminum-gallium oxide thin files on sapphire substrate, *J. Alloys Compd.*, 2018, **765**, 894–900.
- 10 K. C. Shen, C. T. Ku, C. Hsieh, Y. J. Cheng and D. P. Tsai, Deep-ultraviolet Hyperbolic Metacavity Laser, *Adv. Mater.*, 2018, **30**, 1706918.
- 11 S. W. Eaton, M. Lai, N. A. Gibson, A. B. Wong, L. Dou, J. Ma, L. W. Wang, S. R. Leone and P. Long, Lasing in robust cesium lead halide perovskite nanowire, *Proc. Natl. Acad. Sci. U. S. A.*, 2016, **113**, 1993–1998.
- 12 Z. Liang, S. Zhao, Z. Xu, B. Qiao, P. Song, D. Gao and X. Xu, Shape-Controlled Synthesis of All-Inorganic  $\text{CsPbBr}_3$  Perovskite Nanocrystals with Bright Blue Emission, *ACS Appl. Mater. Interfaces*, 2016, **8**, 28824–28830.
- 13 T. M. Brenner, D. A. Egger, L. Kronik, G. Hodes and D. Cahen, Hybrid organic-inorganic perovskites: low-cost semiconductors with intriguing charge-transport properties, *Nat. Rev. Mater.*, 2016, **1**, 15007.
- 14 Y. Zhao and K. Zhu, Organic-inorganic hybrid lead halide perovskites for optoelectronic and electronic applications, *Chem. Soc. Rev.*, 2016, **45**, 655–689.
- 15 S. Sun, D. Yuan, Y. Xu, A. Wang and Z. Deng, Ligand-Mediated Synthesis of Shape-Controlled Cesium Lead Halide Perovskite Nanocrystals via Reprecipitation Process at Room Temperature, *ACS Nano*, 2016, **10**, 3648–3657.
- 16 Y. Wang, M. I. Dar, L. K. Ono, T. Zhang, M. Kan, Y. Li, L. Zhang, X. Wang, Y. Yang, X. Gao, Y. Qi, M. Grätzel and Y. Zhao, Thermodynamically stabilized  $\beta\text{-CsPbI}_3$ -based perovskite solar cells with efficiencies >18%, *Science*, 2019, **365**, 591–595.
- 17 R. Babu, L. Giribabu and S. P. Singh, Recent advances in halide-based perovskite crystals and its optoelectronic applications, *Cryst. Growth Des.*, 2018, **18**, 2645–2664.
- 18 T. J. S. Evans, K. Miyata, P. P. Joshi, S. Maehrlein, F. Liu and X. Zhu, Competition Between Hot-Electron Cooling and Large Polaron Screening in  $\text{CsPbBr}_3$  Perovskite Single Crystals, *J. Phys. Chem. C*, 2018, **122**, 13724–13730.
- 19 J. Tian, Q. Xue, X. Tang, Y. Chen, N. Li, Z. Hu, T. Shi, X. Wang, F. Huang, C. J. Brabec, H. Yip and Y. Cao, Dual Interfacial Design for Efficient  $\text{CsPbI}_2\text{Br}$  Perovskite Solar Cells with Improved Photostability, *Adv. Mater.*, 2019, **31**, 1901152.
- 20 L. Ji, H. Hsu, J. C. Lee, A. J. Bard and E. T. Yu, High-Performance Photodetectors Based on Solution-Processed Epitaxial Grown Hybrid Halide Perovskites, *Nano Lett.*, 2018, **18**, 994–1000.
- 21 Y. Wang, X. Li, S. Sreejith, F. Cao, Z. Wang, M. C. Stuparu, H. Zeng and H. Sun, Photon Driven Transformation of Cesium Lead Halide Perovskites from Few-Monolayer Nanoplatelets to Bulk Phase, *Adv. Mater.*, 2016, **28**, 10637–10643.
- 22 Z. Zhang, Y. Liu, C. Geng, S. Shi, X. Zhang, W. Bi and S. Xu, Rapid synthesis of quantum-confined  $\text{CsPbBr}_3$  perovskite nanowires using a microfluidic reactor, *Nanoscale*, 2019, **11**, 18790–18796.
- 23 Y. Bekenstein, B. A. Koscher, S. W. Eaton, P. Yang and A. P. Alivisatos, Highly Luminescent Colloidal Nanoplates



of Perovskite Cesium Lead Halide and Their Oriented Assemblies, *J. Am. Chem. Soc.*, 2015, **137**, 16008–16011.

24 Z. Zhao, M. Zhong, W. Zhou, Y. Peng, Y. Yin, D. Tang and B. Zou, Simultaneous Triplet Exciton-Phonon and Exciton-Photon Photoluminescence in the Individual Weak Confinement  $\text{CsPbBr}_3$  Micro/Nanowires, *J. Phys. Chem. C*, 2019, **123**, 25349–25358.

25 Z. H. Lin, M. Q. Wang, L. Z. Wei, X. H. Song, Y. H. Xue and X. Yao, PbTe colloidal nanocrystals: Synthesis, mechanism and infrared optical characteristics, *J. Alloys Compd.*, 2011, **509**, 5047–5049.

26 G. Murtaza and I. Ahmad, First principle study of the structural and optoelectronic properties of cubic perovskites  $\text{CsPbM}_3$  ( $\text{M} = \text{Cl}, \text{Br}, \text{I}$ ), *Physica B*, 2011, **406**, 3222–3229.

27 J. J. Urban, D. V. Talapin, E. V. Shevchenko and C. B. Murray, Self-Assembly of PbTe Quantum Dots into Nanocrystal Superlattices and Glassy Films, *J. Am. Chem. Soc.*, 2006, **128**, 3248–3255.

28 J. E. Murphy, M. C. Beard, A. G. Norman, S. P. Ahrenkiel, J. C. Johnson, P. Yu, O. I. Micic, R. J. Ellingson and A. J. Nozik, PbTe Colloidal Nanocrystals: Synthesis, Characterization, and Multiple Exciton Generation, *J. Am. Chem. Soc.*, 2006, **128**, 3241–3247.

29 J. Shamsi, Z. Dang, P. Bianchini, C. Canale, F. Di-Stasio, R. Bresciani, M. Prato and L. Manna, Colloidal Synthesis of Quantum Confined Single Crystal  $\text{CsPbBr}_3$  Nanosheets with Lateral Size Control up to the Micrometer Range, *J. Am. Chem. Soc.*, 2016, **138**, 7240–7243.

30 X. Li, D. Yu, F. Cao, Y. Gu, Y. Wei, Y. Wu, J. Song and H. Zeng, Healing All-Inorganic Perovskite Films via Recyclable Dissolution-Recrystallization for Compact and Smooth Carrier Channels of Optoelectronic Devices with High Stability, *Adv. Funct. Mater.*, 2016, **26**, 5903–5912.

31 G. Hu, X. Cai and Y. Rong, *Fundamentals of materials science*, Shanghai Jiao Tong University Press, Shanghai, 2001.

32 Z. Wu and R. E. Cohen, A More accurate generalized gradient approximation for solids, *Phys. Rev. B: Condens. Matter Mater. Phys.*, 2005, **73**, 235116.

33 H. X. Xiao and C. S. Long, Molecular dynamics simulation of surface energy of low miller index surfaces in  $\text{UO}_2$ , *Acta Phys. Sin.*, 2013, **62**, 103104.

34 B. Viswanath, P. Kundu, A. Halder and N. Ravishankar, Mechanistic Aspects of Shape Selection and Symmetry Breaking During Nanostructure Growth by Wet Chemical Methods, *J. Phys. Chem.*, 2009, **113**, 16866–16883.

35 Q. A. Akkerman, V. D'Innocenzo, S. Accornero, A. Scarpellini, A. Petrozza, M. Prato and L. Manna, Tuning the optical properties of cesium lead halide perovskite nanocrystals by anion exchange reactions, *J. Am. Chem. Soc.*, 2015, **137**, 10276–10281.

36 Y. Yin and A. P. Alivisatos, Colloidal nanocrystal synthesis and the organic-inorganic interface, *Nature*, 2005, **437**, 664–670.

37 S. Lou, T. Xuan, C. Yu and H. Li, Synthesis, Properties and applications of inorganic halide perovskite nanocrystals, *Chin. J. Appl. Chem.*, 2016, **33**, 977–993.

38 Y. Zhao and K. Zhu, Efficient Planar Perovskite Solar Cells Based on 1.8 eV Band Gap  $\text{CH}_3\text{NH}_3\text{PbI}_2\text{Br}$  Nanosheets via Thermal Decomposition, *J. Am. Chem. Soc.*, 2014, **136**, 12241–12244.

39 R. Hoffmann, A chemical and theoretical way to look at bonding on surfaces, *Rev. Mod. Phys.*, 1988, **60**, 601–628.

40 J. M. Zhang, K. W. Xu and F. Ma, Calculation of surface energy of Cu crystal with modified embedded-atom method, *Acta Phys. Sin.*, 2003, **52**, 1993–1999.

